

Network Growth in the Flocculation of Concentrated Colloidal Silica Dispersions

Paul A. Heiney*

*Department of Physics and Astronomy and Laboratory for Research on the Structure of Matter,
University of Pennsylvania, Philadelphia, Pennsylvania 19104*

Robert J. Butera

DuPont Performance Coatings, Marshall Laboratory, Philadelphia, Pennsylvania 19146

J. David Londono, Robert V. Davidson, and Stephen Mazur*

DuPont Research and Development, Wilmington, Delaware 19880

Received: April 25, 2000; In Final Form: June 30, 2000

We have used small-angle X-ray scattering (SAXS) and oscillatory shear rheometry to study the salt-induced flocculation of a concentrated colloidal silica dispersion in water. The SAXS results provided qualitative confirmation of a primary contact coordination shell and barrier as predicted by the DLVO model. The results are consistent with an irreversible, but volume-conserving, growth of a network of interparticle contacts. The activation energy for network growth turns out to be substantially greater than the barrier in the pair potential predicted by the DLVO model, and this difference is ascribed to the importance of multiparticle interactions. The storage modulus of the gel (reflecting the long-range structure) continued to evolve long after changes in the local structure could no longer be distinguished, but ultimately it also converged to a quasi-stationary state. Disruption of the gel network by shear had no detectable effect on the local structure, but caused a dramatic reduction in the moduli which subsequently recovered following different kinetics than in the initial growth process.

1. Introduction

Concentrated suspensions of charge-stabilized colloids may be flocculated by changes in pH or ionic strength into a gel with thixotropic rheology useful for paints, ceramic slips, cosmetics, and foods. While studies of flocculation under highly dilute conditions have revealed some remarkable universal features,¹ those results provide little insight into the complex behavior which arises at high concentrations, especially beyond the gel points.

At high concentrations aggregation and rheological response are both nonuniform functions of time spanning several decades,² the rheology is further complicated by nonlinearity at relatively small strains, and all of these properties are nonlinear functions of particle concentrations.^{3–5} Flocculated gel networks can be partially disrupted by shear^{6–8} and may or may not recover their original properties under quiescent conditions. Some gels undergo syneresis, in which aggregation forces ultimately cause them to shrink and further concentrate by exuding excess solvent. However, syneresis is not universal. Equally common are examples of stationary states where the aggregation process slows and apparently ceases without shrinkage, regardless of the initial concentration.

The structure of colloid clusters grown under dilute conditions apparently depends only on whether the coupling reaction is diffusion-limited or activated.¹ However, details of the interparticle forces undoubtedly play a more prominent role in concentrated colloidal gels than they do for concentrated colloids in general. Understanding the structure may be central to

explaining many of the above phenomena. Evidence from light and X-ray scattering indicates that the structures of both dilute and dense colloids may be fractal in nature^{6–9} and that the fractal dimension may depend on the shear history of the sample.^{6–8} There is little information available, however, on the local structure of the gel or the physical origin of the stationary state.

Earlier studies of flocculated colloidal gels have focused primarily on systems under apparently stationary conditions to determine the effects of compositional parameters such as particle size, volume fraction, pH, and the concentration of electrolytes or steric stabilizers on yield stress and linear viscoelastic properties.^{3–5,10–12} In order to interpret the structure and rheological properties during gelation, it is essential to first distinguish whether those properties represent true stationary states or simply different transient stages in a slowly evolving process. For any given example, it will likewise be important to identify the physical constraints which limit the rate and/or ultimate extent of aggregation. Resolving these issues requires independent kinetic and structural characterization, and the conclusions will necessarily be limited by the sensitivity of the measurements.

We report here a detail study of salt-induced flocculation of colloidal silica dispersions in water. At various stages during initial growth or recovery of the flocculated gel network, small-angle X-ray scattering (SAXS) measurements were used to characterize the local structure and derive the pair distribution function, and linear viscoelastic properties were determined by small-strain oscillatory shear rheometry. The changes in local structure during flocculation were found to be consistent with an activated transition of neighboring pairs from a shallow

* To whom correspondence should be addressed.

secondary minimum into primary contact. While such minima are a feature of the DLVO pair potential,¹³ the potential of mean force which actually governs our experimental kinetics may differ considerably due to effects of multiparticle correlations. It is therefore not surprising that the activation energy for network growth is found to be substantially larger than the barrier predicted by DLVO for coupling of an isolated pair.

The results include several noteworthy features not previously reported. At high salt concentrations, both measurements revealed a progressive autoretardation of the flocculation process and convergence toward a quasi-stationary state. (In the context of rheological measurements, we consider a quasi-stationary state to be one in which the elastic modulus changes less than 1% per hour.) Evolution in the local structure was dominated by a decrease in diameter of the first coordination shell but, surprisingly, the total population at distances encompassing both contact and secondary neighbors did not change greatly. The storage modulus of the gel continued to grow long after changes in the local structure could no longer be distinguished, but ultimately it also converged to a constant value. Disruption of the gel network by shear had no detectable effect on the local structure but caused a dramatic reduction in the moduli which subsequently recovered following a different kinetics than the initial growth process. Possible mechanisms are considered to account for self-limiting network growth consistent with other properties of the system, notably the absence of syneresis.

Experimental details and general characterization are summarized in section 2. The approach taken to the SAXS data analysis is discussed in section 3. Predictions of the DLVO model, and comparison of DLVO predictions to the model used for the SAXS data, are reviewed in section 4. Section 5 describes the SAXS data and analysis of the pair distribution function. Rheological measurements are described in section 6. The relationships and implications of these results are discussed in section 7. The relationships and implications of these results are discussed in section 7. The formalism used in the SAXS data analysis is presented more fully in the Appendix.

2. Experimental Section

All samples were prepared from a single stock of colloidal silica dispersion in deionized water (DIW) prepared according to a proprietary procedure and kindly supplied by Dr. Peter Jernakoff, Dupon Specialty Chemicals. The silica content was 31.7% and density was 1.2091 g/cm³, from which we compute a density of 2.20 g/cm³ and volume fraction $\Phi_v = 0.174$ for the particles. The level of inorganic impurities in this dispersion is much lower than commercial colloidal silicas such as Ludox. Analysis by inductively coupled plasma showed 2 ppm Ca, 0.48 ppm Na, 0.39 ppm Mg, and no other metal ions at greater than 0.1 ppm. The carbon content was 0.15%, much less than colloidal silica prepared via the Stöber process¹⁴ from tetraethyl orthosilicate. The conductivity of <0.2 mmho/cm indicated that background electrolyte concentration was no more than 0.001 M.

Stable dispersions of higher concentration were prepared by dialysis of the stock dispersion against solutions of poly(ethylene glycol), molecular weight 10 000 (Aldrich Chemical Co.) in DIW. For example, dialysis against a 4% solution of poly(ethylene glycol), with osmotic pressure 45.3 kPa,¹⁵ provided a highly viscous, but stable dispersion containing 52.8 wt % silica. Stock solutions of 0.10 M KCl and 1.0 M MgCl₂ in DIW were prepared from analytical reagents and diluted as needed. In studies of the flocculation process, the required quantity of salt-free silica dispersion (from 1 to 5 mL) was added rapidly to a

vial containing a predetermined aliquot of 1.0 M MgCl₂ and mixed vigorously by means of a vibratory mixer or a magnetic stirrer. The sample was then transferred to the rheometer or X-ray sample holder, generally within 1 min.

Preliminary characterization of particle size was obtained from light scattering measurements (Ar ion laser, Brookhaven Instruments BI-200SM goniometer). The radius of gyration, $R_g = 330 \pm 40$ Å, was determined from Guinier analysis of angle-dependent scattering data on a dispersion sample diluted to 0.05% in DIW. Photon correlation spectra (PCS) were determined at an angle of 90° (Brookhaven instruments BI-2030 Digital Autocorrelator). Autocorrelation functions for dispersions with 0.05 wt % silica in 0.001 M KCl indicated nearly monodisperse particles with $R_h = 430 \pm 20$ Å. PCS measurements at electrolyte concentrations ≤ 0.0001 M showed systematically longer correlation times indicative of long-range repulsive interactions between the particles. The ratio $(R_g/R_h)^2 = 0.59$ agrees within experimental error with the theoretical value 0.60 for spheres of uniform refractive index.

The pH of the stock dispersion was 9. Potentiometric titration indicated of pK_a of 8.5 and equivalent weight of 9200. Assuming that this represents SiOH groups on the surface of spheres of radius R_h and density 2.2 g/cm³, it corresponds to 21 ionizable SiOH/nm², which is 2–3 times larger than for typical amorphous silica.¹⁶ This discrepancy indicates that at high pH either charges on the colloid are not restricted to a single atomic layer, or perhaps that Si–O–Si bonds on the surface may undergo partial hydrolysis. Electrokinetic measurements were made using a Zeta potential analyzer, (Zeta-Plus, Brookhaven Instrument Corp., Holtsville, NY). The Zeta potential was –28 mV in unbuffered 0.001 M KCl and increased to –50.7 mV at pH 10.

The stock dispersion ($\Phi_v = 0.174$) exhibits typical characteristics of a charge-stabilized colloid with long-range repulsive interactions. SAXS patterns were dominated by strong Bragg diffraction peaks which could be indexed to an fcc lattice with $\Phi_v = 0.211$. This result closely resembles results of Yoshida et al.,¹⁷ who studied the coexistence of crystalline and amorphous domains in high-purity colloidal silica dispersions and reported a similar difference between the net silica volume fraction and that in crystals. The stock dispersion is a non-Newtonian fluid. It exhibited a power-law viscosity, $\eta = 20 \text{ Pa s } (\dot{\gamma})^{-1}$, corresponding to a Bingham fluid¹⁸ with yield stress of 20 Pa. Both the crystalline diffraction and yield stress were completely suppressed by dilute electrolyte. For example, KCl dispersions at the same Φ_v in 0.002 M KCl exhibited a constant (Newtonian) viscosity of only 0.004 Pa s at strain rates from 0.1 to 100 s^{–1}, and the corresponding SAXS patterns showed only broad peaks characteristic of liquidlike order.

Another measure of interparticle forces was obtained from the variation in osmotic pressure with colloid concentration. Samples of stock dispersion (ca. 2.5 g) were placed in dialysis cassettes (Slide-A-Lyzer, 3500 MWCO, Pierce Chemical Co., Rockford, IL) and allowed to equilibrate at ambient temperature with solutions containing from 1 to 10% by weight of poly(ethylene glycol) (M_w 10 000), whose osmotic pressures had been previously determined.¹⁵ The colloid concentration was calculated from the net mass following an equilibration period of at least 20 h. The data shown in Figure 1 reveal strong interparticle repulsions in the salt-free ordered phase at volume fractions well below the close-packed limit. The osmotic compressibility was found to be reversible (i.e., independent of the concentration history) up to osmotic pressure of about 100 kPa, beyond which the sample failed to swell to its original volume when reequilibrated at lower osmotic pressures.

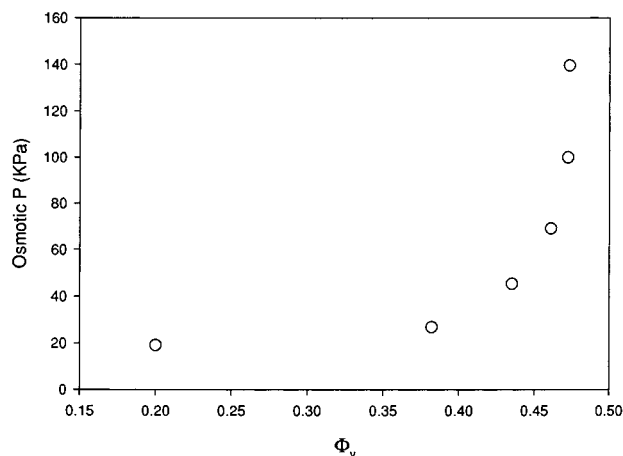


Figure 1. Equilibrium osmotic pressure of silica dispersions in deionized water.

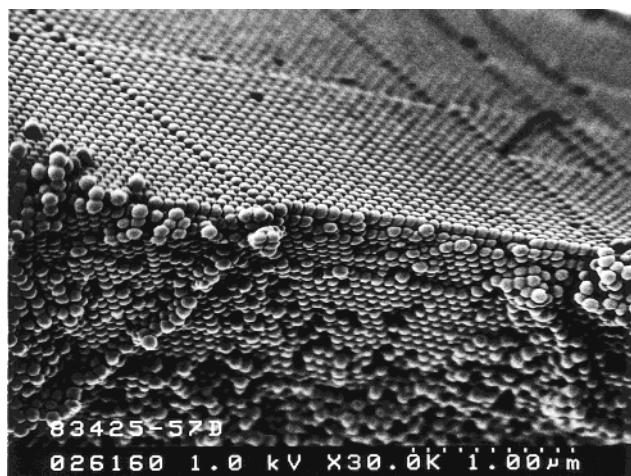


Figure 2. Scanning electron micrograph of dried stock dispersion sample, with no salt. The image shows an area of three by four microns.

A sample of the stock dispersion was allowed to dry, and the resulting solid fragments were examined by scanning electron microscopy. Another manifestation of a narrow distribution of particle sizes is that the majority of particles are organized in dense-packed crystalline domains, as seen in Figure 2.

SAXS measurements were performed at the DND-CAT Synchrotron Research Center, Advanced Photon Source, Argonne National Laboratory. The samples were contained in 1-mm-thick cells with Kapton windows. The cells were mounted on an Instron frame, which provided X-Y translation for sample alignment. The energy to the X-ray beam from an insertion device (ID) was tunable from 7 to 18 keV. The ID, double crystal monochromator, first, second, and third set of adjustable slits, and the sample were located at 0, 30, 35, 54, 66, and 68 m, respectively, along the X-ray beam path from the synchrotron orbit. The size of the square beam was defined at the first and second sets of slits, which were both set to 100 μm . A parasitic scattering slit, having the shape of a round pinhole only large enough to circumscribe the square beam, was placed 1–2 mm before the sample. A circular lead beamstop 2 mm in diameter was placed immediately before the detector. The two-dimensional CCD (Mar) detector had 2048×2048 pixels with a 16-bit intensity scale and a circular active area of 133 mm diameter. In all cases the detector was used in a 4×4 binning mode at a resolution of 512×512 , with effective pixel size $258 \mu\text{m}/\text{pixel}$. We note that, in addition to the normal counting statistics, the CCD detector introduces additional readout noise, on the

order of 1 photon per pixel. It was important to explicitly take this into account when analyzing the data, since it introduced a source of noise that was independent of the detector integration time. The detector was placed at the end of an evacuated 8 in. pipe fitted with Kapton windows on both ends. The sample to detector distance was adjustable from a few centimeters to 8.5 m. For the measurements reported here, the detector was placed at a distance of 8.496 m away from the sample and the ID was tuned to an energy of 8.048 KeV, corresponding to a wavelength $\lambda = 1.541 \text{ \AA}$. At this distance the detector covered scattering angles 2θ corresponding to the range in the scattering vector magnitude $8 \times 10^{-4} < q (=4\pi/\lambda) \sin \theta < 3 \times 10^{-2} \text{ \AA}^{-1}$.

With this configuration it was possible to collect an entire spectrum in less than 1 min (essential for observing the time evolution early in the process of flocculation), and with sufficiently high resolution that it was not necessary to desmear the data.

After data collection, a circular numerical average was performed on each data set to provide a set of intensities versus momentum transfer magnitude $|\vec{q}|$. The numerical values of these intensities were proportional to the number of photons scattered at that angle. The magnitude of the Poisson error was established by comparing short segments of 10 data points to a best-fit cubic spline curve. Each entire data set, including estimated Poisson errors, was then least-squares fit to an empirical model for the intensity as discussed in section 3.

Rheological experiments were performed using a Rheometrics RFSII fluids spectrometer equipped with parallel plate or couette fixtures and a force rebalance torque transducer. Oscillatory shear measurements were used to determine G' , the storage modulus, and G'' , the loss modulus, as a function of frequency, and as a function of time at fixed frequency. Experiments were conducted by applying a sinusoidal strain and measuring the phase angle of the induced sinusoidal stress response. This stress response was then decomposed into signals that are in-phase and out-of-phase with the strain input; G' is proportional to the in-phase (elastic) portion and G'' is proportional to the out-of-phase (viscous) portion.¹⁹ All experiments were performed in the linear viscoelastic region, where the moduli are independent of the applied strain amplitude. Linear viscoelasticity was ensured by evaluating the strain dependence of the moduli at individual frequencies and then operating at small strains where the moduli were strain independent. Temperature was controlled using a circulating water bath. Evaporation of water from the sample was prevented using a small-volume, close-fitting clamshell cover lined with absorbent material, which was saturated with water.

3. Analysis of SAXS Results

A detailed discussion of the SAXS data analysis is provided in the Appendix. Here we summarize the important features of our model. In general, the scattered X-ray intensity is given by

$$I(\vec{q}) = I_0 S(\vec{q}) |F(\vec{q})|^2 \quad (1)$$

$$S(\vec{q}) = \left| \sum_i e^{i\vec{q} \cdot \vec{r}_i} \right|^2 = \sum_i \sum_j e^{i\vec{q} \cdot (\vec{r}_i - \vec{r}_j)} \quad (2)$$

$$F(\vec{q}) = \int d^3r e^{i\vec{q} \cdot \vec{r}} f(\vec{r}) \quad (3)$$

where \vec{r}_i is the position of the i th particle and $f(\vec{r})$ describes the charge distribution around a reference site \vec{r} . We used a form $F(\vec{q})$ appropriate to weakly polydisperse spheres with radius R_0 and dispersion σ_0 ²⁰

$$|F(q)|^2 = \frac{1}{\sigma_b \sqrt{2\pi}} \int dr e^{-(r-R_b)^2/2\sigma_b^2} \left| \frac{4\pi r^3 \rho_0}{3} \mathcal{R}(q, r) \right|^2 \quad (4)$$

$$\mathcal{R}(q, r) \equiv 3 \frac{\sin(qr) - (qr) \cos(qr)}{(qr)^3} \quad (5)$$

The structure factor $S(q)$ is given by the Fourier transform of the two-particle density correlation function $g(r) \equiv 1 + h(r)$:

$$S(\vec{q}) = \langle n \rangle (1 + \langle n \rangle \int d^3r e^{i\vec{q} \cdot \vec{r}} h(\vec{r})) \quad (6)$$

where $\langle n \rangle$ is the average particle density.

In analyzing SAXS data, several common approaches are commonly taken to factoring out $|F(\vec{q})|^2$ from $S(\vec{q})$ in eq 1:

1. In some cases, one is primarily interested in determining the structure of individual particles.^{21–25} In the limit of infinite dilution, $S(q) \rightarrow 1$, and interparticle correlations can be ignored. More realistically, one can measure a series of samples of increasing dilution and try to establish the limit of $S(q) \rightarrow 1$. As we shall see, however, even at 1% dilution the interparticle correlations can have a noticeable effect on the scattered intensity. One can also concentrate on higher- q data, on the principle that long-distance correlations will be manifested primarily at low q , or one can attempt to factor out the $S(q)$ contribution by calculating the structure expected for hard spheres or other simple models.²²

2. In some cases, the colloid has crystallized, and sharp peaks appear in $S(q)$. In this case, it may be sufficient to establish the crystal space group and lattice spacing by measuring the positions of the peaks, without attempting a quantitative analysis of the intensity.^{25–28}

3. To quantitatively determine $S(q)$, the simplest approach is to make measurements at high dilution and then divide the higher concentration scattering patterns by the dilute pattern.^{29,30} The risk here is that structure factor effects may be important even at high dilution. Additionally, considerable noise is introduced when dividing the data point-by-point near the minima in $F(q)$.

4. For relatively small particles, the minima in $|F(q)|^2$ are pushed out to relatively large q . In this case, one can attempt to establish the form of $|F(q)|^2$ (usually using an empirical line shape) at large q , then divide $I(q)$ by $|F(q)|^2$ to obtain $S(q)$ directly.^{26,31,32} This procedure will be most accurate at very small values of q where $|F(q)|^2$ does not vary rapidly.

5. In some cases, however, one finds that the interesting length scale of interparticle correlations is comparable to the size of the particles. In this case, one cannot obtain a clean separation of $S(q)$ and $|F(q)|^2$. Additionally, dividing $I(q)$ by $|F(q)|^2$ to obtain $S(q)$ can suffer from the difficulty that the first maximum in $S(q)$ is “accidentally” at a minimum in $|F(q)|^2$. In this case, an alternate approach is to compare the entire diffraction pattern to a structural model incorporating free variables in both the particle size and $g(r)$, either by using a Monte Carlo approach³³ or via least-squares fits of the measured intensity to the entire $I(q)$ function, including free variables in both $|F(q)|^2$ and $S(q)$.³⁴ The latter is the approach we took in our analysis.

For $|F(q)|^2$ we used the smeared Rayleigh function presented in eqs 4 and 5. For the structure factor, we chose an empirical function for $g(r)$ which contained the appropriate physical constraints, then calculated $S(q)$ using a combination of analytical and numerical Fourier transforms. $g(r)$ was parametrized such that there was a depletion “well” for $0 \leq r \leq R_w$, where

R_w is the radius of the depletion well, with depth determined by the volume fraction Φ_v and edge sharpness σ_w , and two Gaussian peaks representing coordination shells with radii R_1 , R_2 , widths σ_1 , σ_2 , and coordination numbers c_1 , c_2 . The resulting $g(r)$ qualitatively resembles those calculated from analytical theories for equilibrium structures, such as DLVO theory¹³ or the hypernetted chain equation.³⁵ It should be emphasized, however, that, despite the physical rationalization of introducing parameters such as R_w , in the final analysis the form of $g(r)$ was purely empirical, and the fitted parameters are less meaningful than the positions of maxima, minima, etc., in the optimized $g(r)$.

The formula used is given by

$$I(q) = \sqrt{(Bb(q))^2 + C^2} + A \frac{1}{\sqrt{\pi}} \sum_{i=1}^n w_i \left| \frac{4\pi(R_b + \sqrt{2}\sigma_b x_i)^3}{3} \rho_0 \mathcal{R}(q, R_b) + \sqrt{2}\sigma_b x_i \right|^2 \left(1 - \frac{\Phi_v}{\sqrt{\pi}} w_i \mathcal{R}(q, R_w + \sqrt{2}\sigma_w x_i) + \frac{c_1}{\sqrt{\pi}(R_1^2 + \sigma_1^2)} \sum_{i=1}^n (R_1 + x_i \sigma_1) \frac{\sin q(R_1 + x_i \sigma_1)}{q} w_i + \frac{c_2}{\sqrt{\pi}(R_2^2 + \sigma_2^2)} \sum_{i=1}^n (R_2 + x_i \sigma_2) \frac{\sin q(R_2 + x_i \sigma_2)}{q} w_i \right) \quad (7)$$

as derived in the Appendix. Here q is the momentum transfer, B and C are arbitrary background prefactors, $b(q)$ is an empirical polynomial describing the background scattering, A is an arbitrary intensity prefactor, R_b is the ball radius, σ_b describes the polydispersity of ball radii, R_w is the radius of the depletion well sphere, σ_w is the width of the “wall” of the depletion sphere, Φ_v is the volume fraction of colloidal spheres, R_1 , c_1 , and σ_1 are the radius, coordination number, and width of the first coordination shell, R_2 , c_2 , and σ_2 are the radius, coordination number, and the width of the second coordination shell, and x_i and w_i are the positions and widths used in the Hermite integration algorithm. In the final round of fits, as many parameters as possible were constrained to be equal to their average values. For example, we required that the ball radius be the same for all measured concentrations.

4. Review of DLVO Predictions and Comparison with the Empirical SAXS Model

To test our fitting algorithm, we created “simulated” data using the DLVO pair potential. The DLVO potential $u(r)$ is considered to be the sum of screened electrostatic and dispersion contributions u_e and u_d . Following Russel et al.,³⁶ we employ the linear superposition approximation for the former and the Hamaker approximation for the latter:

$$u_e = \frac{4\pi\epsilon_0 R^2}{s + 2R} \psi_s^2 e^{-\kappa s} \quad (8)$$

$$u_d = -\frac{A_{\text{eff}} R}{s} \quad (9)$$

where $\epsilon_0 = 7.08 \times 10^{-10} \text{ C}^2/\text{N m}^2$ is the permittivity of water, $R = 440 \text{ \AA}$ is the particle radius, s is the distance between

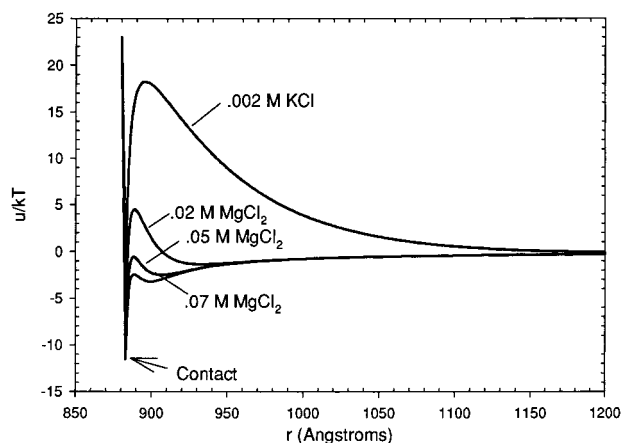


Figure 3. DLVO pair potentials calculated (eq 10) for $\psi_s = 26$ mV, $R_b = 440$ Å, and the indicated salt concentrations.

particle surfaces (in Å), ψ_s is the surface potential, and $\kappa(\text{Å}^{-1}) = 2.32 \times 10^7 \text{ cm}^{-1} (\sum z_i^2/M_i)^{1/2}$ is the inverse Debye length. $A_{\text{eff}} = 0.83 \times 10^{-20}$ J is the effective Hamaker coefficient for silica in water. Recasting this as a function of the distance between particle centers, $r = 2R + s$, at $T = 298$ K we obtain

$$\frac{u}{kT} = 0.141 \text{ Å}^{-1} \left(\frac{R^2}{r} \right) \left(\frac{e\psi_s}{kT} \right)^2 e^{-\kappa(r-2R)} - \frac{0.213R}{r-2R} \quad (10)$$

Figure 3 shows examples of DLVO pair potentials calculated for various salt concentrations employed in our experiments. In the limit of dilute particles, the equilibrium pair distribution $g(r)$ may be approximated by $\exp(-u(r)/kT)$. This approximation provides a convenient means to test the reliability of our SAXS analysis, and is valid for comparison with experimental data at high dilution, but is clearly inappropriate for data at the higher concentrations of interest in this study.

Figure 4a shows examples of dilute $g(r)$ for 0.002 M KCl and 0.05 M MgCl_2 simulated according to the dilute DLVO approximation. (They extend to $r_{\text{max}} = 2500$ Å where $g(r) \approx 1.0$.) A small adjustment was made to $h(r)$ in order to eliminate truncation artifacts in the Fourier transforms, giving

$$h'(r) = e^{-u(r)/kT} - e^{-u(r_{\text{max}})/kT} \quad (11)$$

Scattering functions were then calculated assuming particles with mean radius 440 Å and a dispersion 13 Å:

$$S(q) = \sum_i h'(r) \frac{r_i \sin(qr_i)}{q} \Delta r \quad (12)$$

$$I(q) = A|F(q)|^2(1 + 4\pi DS(q)) + Bb(q) + C \quad (13)$$

The simulated $I(q)$ (Figure 4b, symbols) were calculated over the interval $0.002 \text{ Å}^{-1} < q < 0.035 \text{ Å}^{-1}$ and compared with least-squares fits generated following the algorithm described in section 3 (Figure 4b, solid lines). The best-fit values of $g(r)$ derived from this analysis are shown in Figure 4c. In reciprocal space, the simulated data and empirical model are indistinguishable (Figure 4b). The fitted ball radius and dispersion were almost identical with the inputs to the simulation. The background parameters were of the same order of magnitude, but were slightly different. The biggest discrepancy was in the values of Φ_V , which differed by up to a factor of 3 (e.g., 0.05 in the simulation vs 0.014 in the fit). This indicates that the model compensates for other discrepancies in $S(q)$ by adjusting the volume fraction.

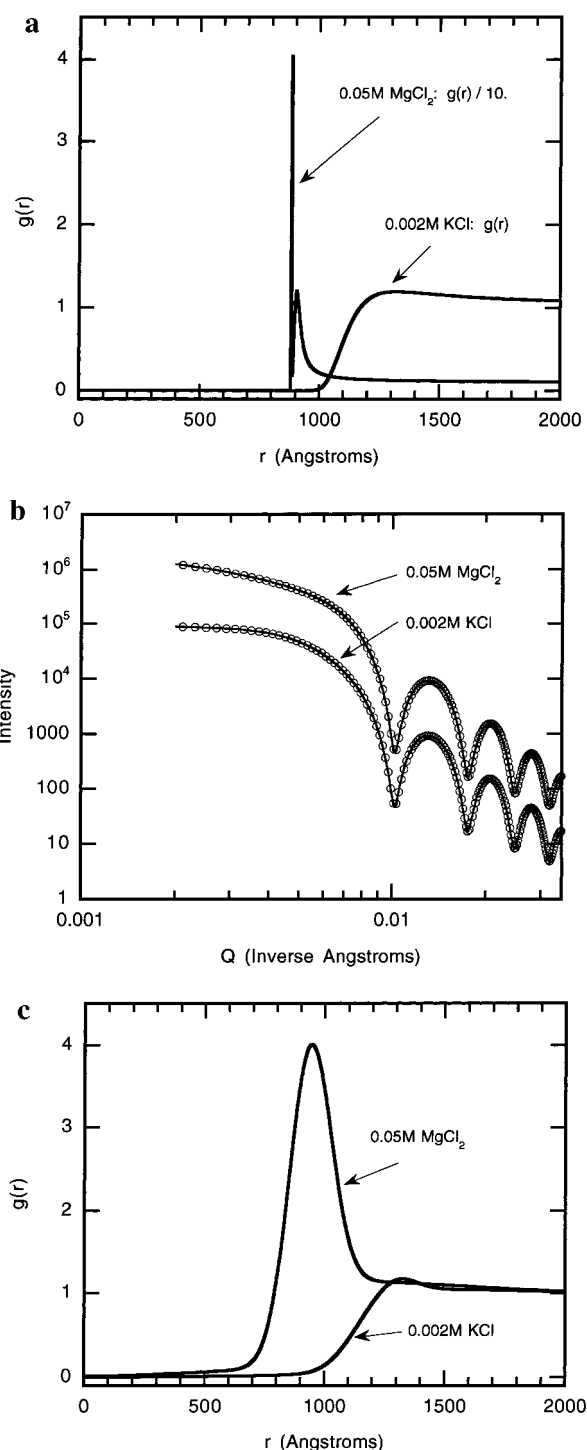


Figure 4. (a) Simulated $g(r)$ models corresponding to DLVO theory for a 5% SiO_2 sample in the presence of 0.05 M MgCl_2 or 0.002 M KCl. (b) Simulated SAXS data (circles) and model (curve) for 5% SiO_2 sample in the presence of 0.05 M MgCl_2 or 0.002 M KCl. For clarity, only every tenth data point is shown, and curves are offset along the intensity axis by a factor of 10. The simulated data were constructed by calculated $g(r)$ from the DLVO potential, adding an empirical background and calculating the Fourier transform (eq 13). These simulated data were then fit with the same model used for the “real” data. (c) The real space $g(r)$ models corresponding to the fitted parameters from the simulated data shown in (b).

This exercise confirms that the algorithm is capable of fitting realistic scattering data to well within experimental error, and also illustrates an intrinsic limitation in the data. We note that the $g(r)$ derived from the fits (Figure 4c) recover the broad features of the original input (Figure 4a), but they fail to resolve

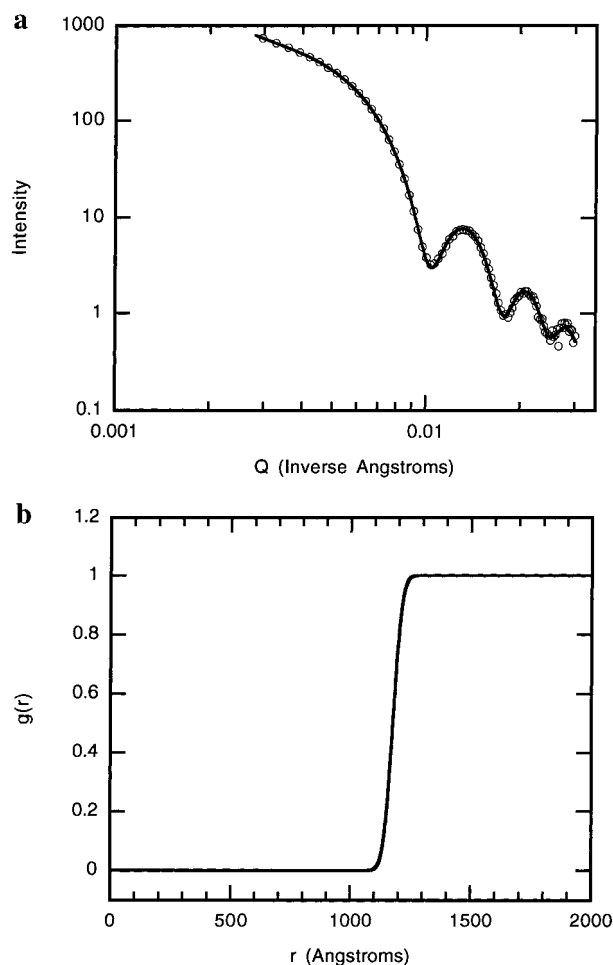


Figure 5. (a) SAXS data (circles) and model (curve) for a 1% SiO₂ sample in the presence of 0.002 M KCl. Only every tenth data point is shown. The model function had a particle-shape factor $|F(q)|^2$ times an empirical structure factor $S(q)$, as described in the text. The fits employing models with and without the depletion well are indistinguishable by eye, but statistically distinguishable. (b) The real space $g(r)$ corresponding to the model incorporating a depletion zone, used in analyzing the 1% data shown in (a).

the sharp peak at $r = 2R_b$ in the latter corresponding to particles trapped in the primary minimum of the DLVO potential. This loss of resolution is primarily a consequence of the limited range of q retained in the transform, a limit which was chosen to conform to our experimental data. Thus, the minimum peak width in Figure 4c is comparable to the minimum wavelength of the transform, ca. 180 Å. It is apparent that in order to distinguish any fine structure in $g(r)$, scattering data would need to extend to $q \sim 0.35 \text{ Å}^{-1}$. We also note that systematic errors in Φ_V obtained from least-squares fits to real data may be substantial.

5. SAXS Results

Figure 5 shows the SAXS pattern and corresponding $g(r)$ for a 1% SiO₂ sample in the presence of 0.002 M KCl. The model used to fit the data for this highly dilute sample incorporated a depletion well but no coordination shell. The fitted parameters were $R_b = 434 \pm 1 \text{ Å}$, $\sigma_b = 12.4 \pm 5.0 \text{ Å}$, $\Phi_V = 7.8 \times 10^{-3} \pm 4 \times 10^{-4}$, $R_w = 1177 \pm 80 \text{ Å}$, and $\sigma_w = 30 \pm 500 \text{ Å}$ (i.e., any $\sigma_w \leq 530 \text{ Å}$ gave a good fit). The ball radius is consistent with that obtained from quasi-elastic light scattering (QELS). The small value of σ_b indicates that this sample was highly monodisperse. The depletion zone radius R_w is slightly greater

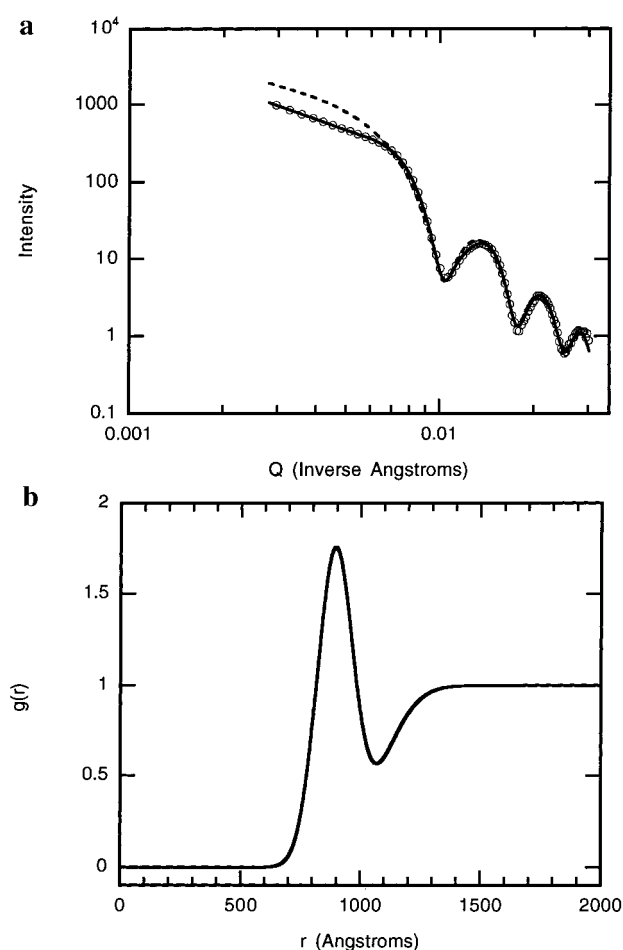


Figure 6. (a) SAXS data (circles) and model for a 31.7 wt % SiO₂ sample in the presence of 0.020 M MgCl₂. Only every tenth data point is shown. This sample was resheared immediately before making the measurement. Solid curve shows a model with the full $S(q)$ (including a contact Gaussian peak and depletion well); dashed curve shows the single-particle form factor plus background only. (b) The real space $g(r)$ corresponding to the model incorporating both the depletion zone and the nearest-neighbor contact peak, used in analyzing the data shown in (a).

than $2R_b$, as expected. The volume fraction of silica spheres, Φ_V , was within error bars of that calculated from the known density and mass fraction. The χ^2 goodness-of-fit parameter for a model that did not incorporate the depletion well was significantly larger than that for a model that did incorporate the well ($\chi^2 = 11.0$ vs 7.5), although the fits are virtually indistinguishable by eye.

Figure 6 shows SAXS data from a sample with 31.7 wt % SiO₂ in the presence of 0.020 M MgCl₂. This sample had been vigorously resheared immediately before the measurement was made.³⁷ Two models were used to fit the data: the full expression in eq 7 with a depletion region and one Gaussian peak, and the smeared spherical particle form factor alone. It can be seen that the full expression provides a good representation of the data, and in fact is almost indistinguishable from the data, while the form factor model alone deviates significantly from the data at low q .

For the fit shown in Figure 6, the ball radius and dispersion were held fixed at $R_b = 434 \text{ Å}$ and $\sigma_b = 10 \text{ Å}$ (the average values from many samples) and the volume density was held fixed at $\Phi_V = 0.28$ (if allowed to vary the error bar was ± 0.02). The exclusion volume radius and width converged to $R_w = 1080 \pm 100 \text{ Å}$ and $\sigma_w = 120 \pm 100 \text{ Å}$. The coordination number,

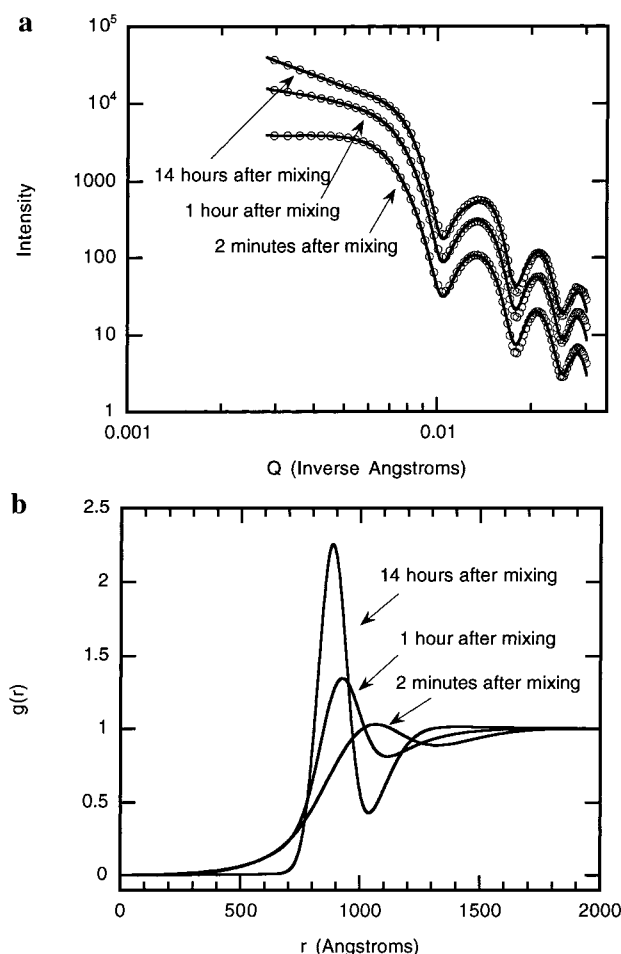


Figure 7. (a) SAXS intensity and model for a 31.7 wt % SiO_2 sample in the presence of 0.050 M MgCl_2 at indicated times after mixing. For clarity, only every tenth data point is shown, and scans are offset along the intensity axis. (b) The real space models used in analyzing the data shown in (a).

radius, and width of the Gaussian peak converged to $c_1 = 3.7 \pm 1.0$, $R_1 = 894 \pm 25$ Å, and $\sigma_1 = 75 \pm 30$ Å. Note that R_1 is almost exactly equal to the value expected for two balls of radius 434 Å in close contact. The good agreement between the model and the data gives us some confidence that the basic features of the model are correct. On the other hand, there is an inconsistency between the fitted Φ_V of 0.28 (obtained from the fitted depth of the well) and the value of 0.17 calculated from the known density and weight fraction of the sample. As discussed above, it is likely that our empirical model is compensating for features of the true $g(r)$ that were not incorporated in the model by adjusting the well depth. This provides a cautionary indication that, although the nearest-neighbor coordination peak almost certainly exists, and is of the same order of magnitude as the value we calculate, the “true” value may differ by $\sim 30\%$.

By contrast, substantial evolution was seen in samples which were freshly prepared immediately before the SAXS measurement. Figure 7 shows the beginning, intermediate, and end points of measurements on a freshly prepared 31.7 wt % sample in the presence of 0.050 M MgCl_2 . These fits were marginally improved by the addition of a second, very broad Gaussian peak. The most dramatic change in the raw data (Figure 7a) is the change in slope at low q , and its most dramatic manifestation in real space is seen in the change in peak height and sharpness of the nearest-neighbor contact peak (Figure 7b).

This trend is summarized in Figure 8, which shows the parameters arising from the least-squares fits. (For these fits the ball radius was fixed at $R_b = 434$ Å, the ball radius dispersion was fixed at $\sigma_b = 13$ Å, the volume density was fixed at $\Phi_V = 0.283$, the radius of the second Gaussian peak was fixed at $r_2 = 1125$ Å, and the width of the second Gaussian peak was fixed at $\sigma_2 = 450$ Å.) The nearest-neighbor coordination (Figure 8a) can be represented in two ways. The parameter c_1 (solid circles), representing the integrated intensity under the first Gaussian peak in the model, increases slightly after about 100 min, but the increase is comparable to the error bars. A somewhat better measure of the first-shell coordination is provided by a numerical integral of the total (empirical) $g(r)$:

$$I_1 = \int_0^{r_{\min}} 4\pi r^2 \langle n \rangle g(r) dr \quad (14)$$

where r_{\min} is the position of the first minimum in $g(r)$. As shown by the triangles in Figure 8a, I_1 actually *decreases* after 30–60 min. This decrease is accompanied by a decrease in the mean radius of the first coordination shell (Figure 8b) and the width of the first shell (Figure 8c).

These changes all correspond to the development of a much better-ordered structure on the 1500 Å length scale. At short times, a disordered local structure leads to a poorly defined coordination shell. As the order increases, particles either “fall into” the first shell or are pushed out to larger distances, resulting in a sharper coordination shell with a slightly smaller total number of particles. We will associate the 60–120 min time period over which this takes place with the “induction” period observed in our rheology measurements, as discussed in section 6.

Similar effects were seen in a more concentrated sample. Figure 9 shows the SAXS intensity, fit, and $g(r)$ obtained from a 53.7 wt % SiO_2 sample in the presence of 0.020 M MgCl_2 . The SAXS pattern changes subtly but noticeably at low q , corresponding to a sharpening of $g(r)$ with increasing time. These data were well described by the same form factor used in analyzing the 31.7% data: a depletion well, a narrow peak of width 80–100 Å, and a broad peak of width $\sigma_2 \approx 760$ Å centered around $r_2 \approx 1400$ Å. The volume density obtained from the fits was $\Phi_V = 0.496$, to be compared with the value of 0.345 obtained from the sample preparation parameters. Figure 10 shows the positions of the first maximum in $g(r)$, first minimum in $g(r)$, and coordination number I_1 as a function of time after mixing with salt. The shell sharpens and moves to somewhat smaller radius, with a modest decrease in coordination number, over the first 20 min. At longer times no significant changes were observed.

By contrast, SAXS patterns of “resheared” samples, in which the solution was prepared several days in advance of the experiment and then sheared³⁷ immediately before the SAXS measurement, all had a qualitative resemblance to the long-time pattern in Figure 7 and the resheared pattern shown in Figure 6. No change was ever observed in the SAXS patterns of resheared samples, on time scales from 2 min to 24 h. Evidently, the local structure (on a length scale of $0 \rightarrow 1500$ Å) is unaffected by the shear due to injection through a hypodermic needle. Presumably, reshearing the sample breaks apart clusters but does not greatly affect the short-range order, so there is no induction stage in the rheology (see section 6) and the SAXS pattern is time-independent.

An unexpected outcome of our analysis was the observation that the SAXS intensity at quite low angles was still described by a model incorporating correlations up to only 1500 Å. It is

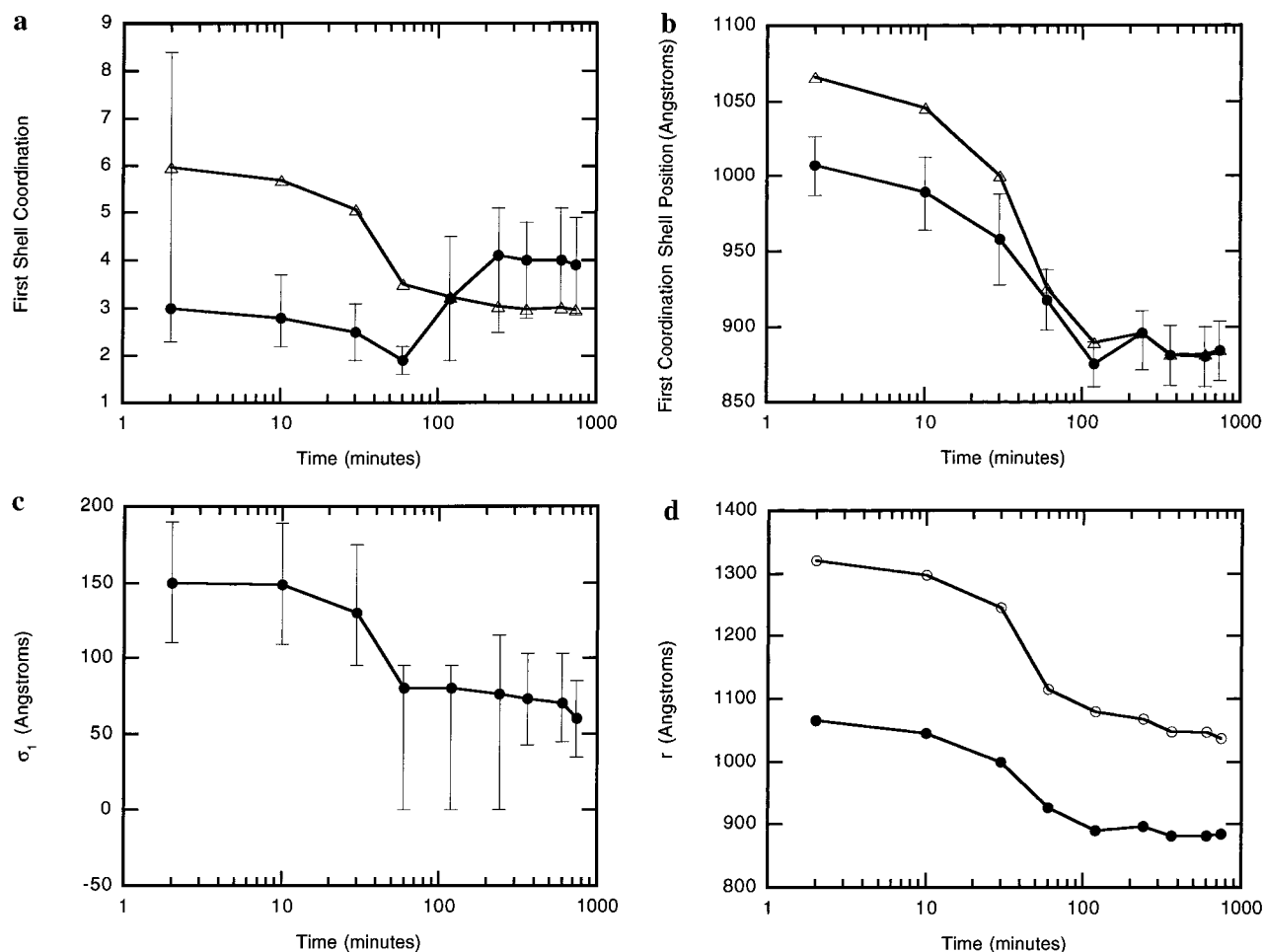


Figure 8. Fitted parameters from time-series data for a 31.7 wt % SiO₂ sample in the presence of 0.050 M MgCl₂. In all cases, error bars were obtained by systematically varying parameters and estimating the region over which acceptable fits were obtained. (a) First shell coordination number. Solid circles and error bars show the fitting parameter c_1 , corresponding to the integrated intensity under the first Gaussian peak, while open triangles show the numerically integrated coordination I_1 (eq 14). (b) Center position of first coordination shell. Solid circles and error bars show the fitting parameter R_1 , corresponding to the center of the first Gaussian peak, while open triangles show the position of the first maximum in $g(r)$. This may differ from R_1 due to overlap with the edge of the “depletion well.” (c) Width σ_1 of the first Gaussian peak, with error bars. (d) Position of the first maximum in $g(r)$ (solid circles) and first minimum in $g(r)$ (open circles).

common to assert^{38–40} that there are three important regimes in a SAXS pattern. In the Guinier regime, when $q < 1/\xi$ (where ξ is the correlation length of the clusters), the scattering should be only weakly dependent on q , due to the density homogeneity on sufficiently large length scales. The fractal regime^{7,9,34,38–41} with $1/\xi < q < 1/R_b$ arises from the self-similarity of colloidal clusters, as reflected in a power-law dependence of $S(q)$ on q . In the Porod regime, with $q > 1/R_b$, the scattering originates from the surface of particles, i.e., is completely dominated by the size and shape of the individual particles. However, as previously observed,^{34,41} the intermediate regime where $qR_b \sim 1$ can also be important, and it is essential to separate the different length scales. The low-angle regimes of Figure 7a and Figure 9a appear to have powerlaw behavior, but in fact are well-described by a local model incorporating nearest-neighbor correlations only. This does not mean that there are no fractal correlations on longer length scales, but it does imply that one should use extreme care when interpreting low-angle power-law behavior in $I(q)$ as arising from fractal behavior.

Our results are similar to those of Hanley et al.,^{6–8} in that we see a significant increase in the scattering at low q as a function of time after gellation is initiated. Since their particles were much smaller than ours (70 Å instead of 440 Å), they were able to probe larger distances r compared to the ball radius R_b , but were less sensitive to the near-neighbor correlations.

6. Dynamic Rheology Results

Small-amplitude oscillatory shear rheometry was used to study the continuum properties of the colloid at various stages in the flocculation process and during structural recovery following steady shear of previously flocculated samples. A range of silica and salt concentrations was investigated, including conditions equivalent to the SAXS experiments. A more extensive characterization was provided by rheological measurements at higher concentrations, which resulted in higher moduli and rates of flocculation.

Figure 11 shows the moduli during flocculation for samples at 48.5 and 53.7 wt % silica, both containing 0.070 M MgCl₂. The rheological evolution of the 48.5 wt % samples shows three distinct regimes: an initial “induction” period, a fast-growth regime, and a final “quasi-stationary state” regime where the modulus growth slows substantially. The growth rate of G' in the fast-growth regime is 18 dyn/(cm²·s), slowing to less than 1 dyn/(cm²·s) in the quasi-stationary state regime. As expected, the sample at higher particle concentration possesses a significantly higher growth rate in the fast-growth regime (270 vs 18 dyn/(cm²·s)), as well as a shorter induction period (which can be seen clearly in the inset on Figure 11).

At high silica concentrations the rheology measurements were limited by the compliance of the instrument. Figure 12 compares

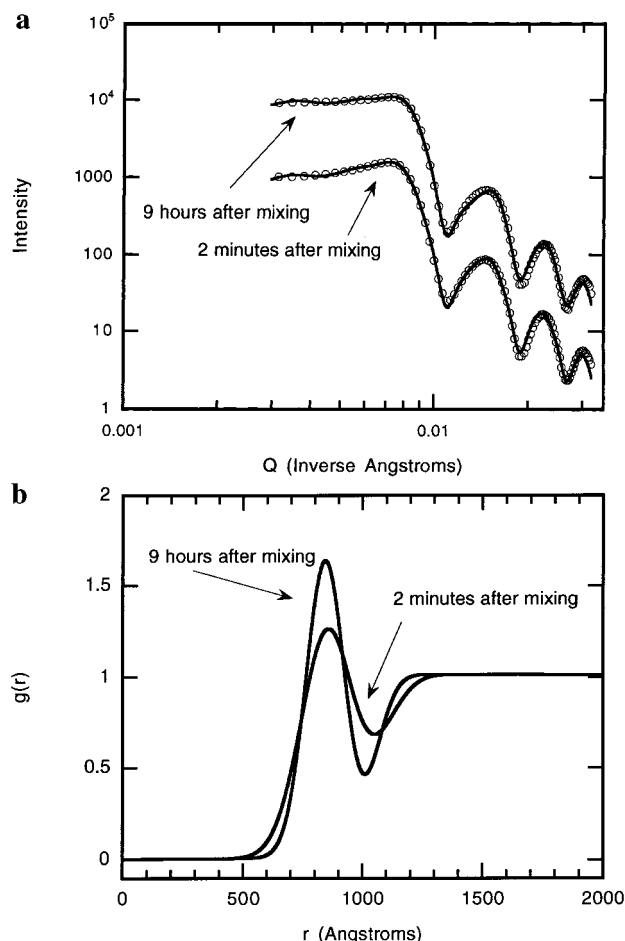


Figure 9. (a) SAXS data (circles) and model for a 53.7 wt % SiO_2 sample in the presence of 0.020 M MgCl_2 , at indicated times after mixing. For clarity, only every tenth data point is shown, and scans are offset along the intensity axis. (b) The real space models used in analyzing the data shown in (a).

the early-time behavior of samples of 53.7 wt % silica at MgCl_2 concentrations of 0.05 M and 0.07 M. Again, the expected behavior is observed, with the sample containing the higher salt concentration exhibiting a higher rate in the fast-growth regime (270 vs 85 $\text{dyn}/(\text{cm}^2\cdot\text{s})$) and a shorter induction phase.

If a gelled sample was sheared and the structure allowed to re-form, it is not obvious that the same kinetics and ultimate structure should be observed as for the case of de novo flocculation. To investigate this issue, the 53.7 wt % silica/0.070 M MgCl_2 sample which was used to produce the data shown in Figure 13 was sheared and the gel formation was subsequently monitored in the same way as for the de novo case. The sample was sheared sequentially for 60 s at 0.05 s^{-1} and then for 60 s at 0.1 s^{-1} immediately prior to the initiation of the oscillatory shear experiment. This sequential shearing was necessary to prevent damage to the rheometer transducer that could result from instantaneous application of a high steady shear rate to a gelled sample with high modulus. Approximately 100 min elapsed between the start of the de novo flocculation and the start of oscillatory shear experiment after steady shear (including the time to shear the sample). This figure shows that the growth of the network after shear is substantially faster than the growth due to initiation of flocculation (270 $\text{dyn}/(\text{cm}^2\cdot\text{s})$ after initiation of flocculation vs 560 $\text{dyn}/(\text{cm}^2\cdot\text{s})$ after shear). In addition, the resheared sample does not show the induction period characteristic of the de novo flocculation.

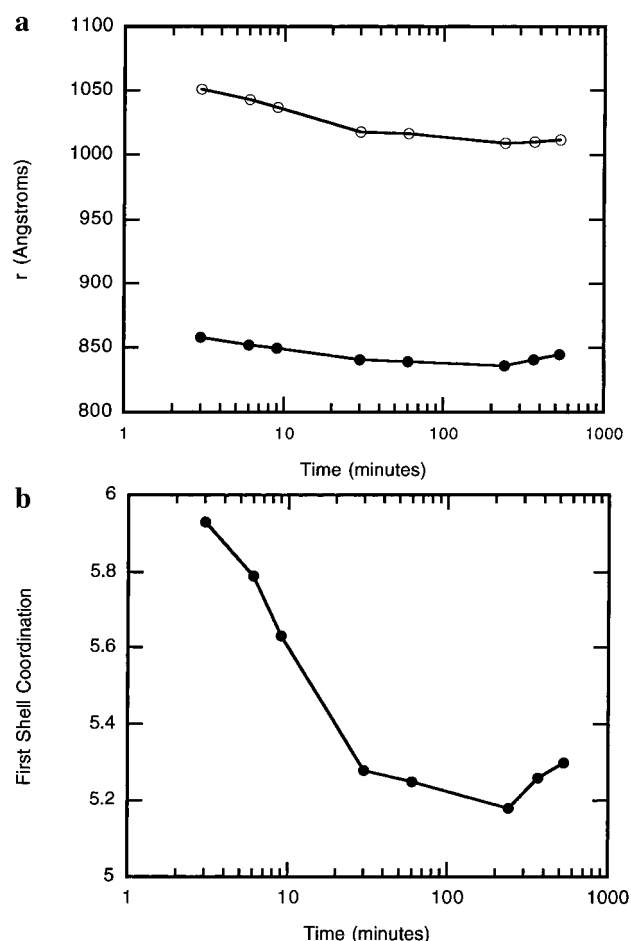


Figure 10. Numerically extracted parameters from time-series data for a 53.7 wt % SiO_2 sample in the presence of 0.020 M MgCl_2 . (a) Position of the first maximum in $g(r)$ (solid circles) and first minimum in $g(r)$ (open circles). (b) Numerically integrated coordination number I_1 (eq 14).

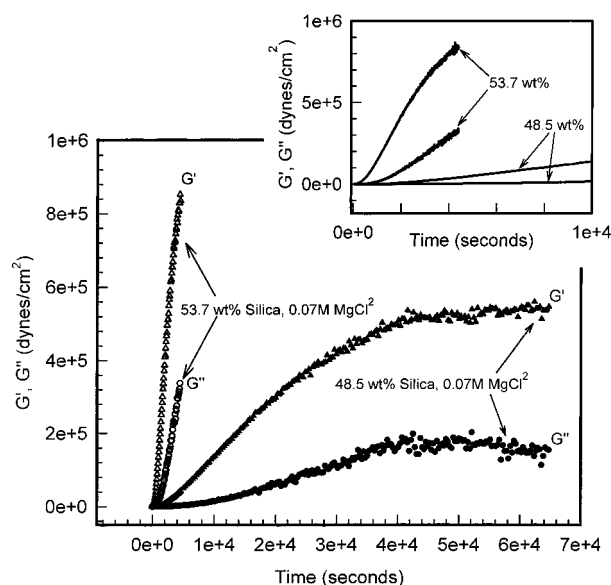


Figure 11. Storage modulus (triangles) and loss modulus (circles) recorded at a frequency of 10 rad/s for 48.5 wt % (filled symbols) and 53.7 wt % (open symbols) SiO_2 samples in the presence of 0.07 M MgCl_2 , as a function of time after mixing the particles with MgCl_2 solution. Inset: scale expansion of the early time region.

The growth of G' at late stages is nearly identical with that from the sample during de-novo flocculation. For instance, if

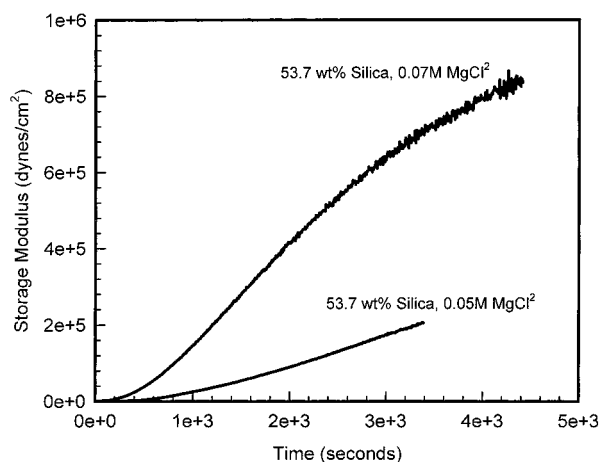


Figure 12. Storage modulus recorded at a frequency of 10 rad/s for 53.7 wt % SiO₂ samples in the presence of 0.07 M MgCl₂ and 0.05 M MgCl₂ as a function of time after mixing the particles with MgCl₂ solution.

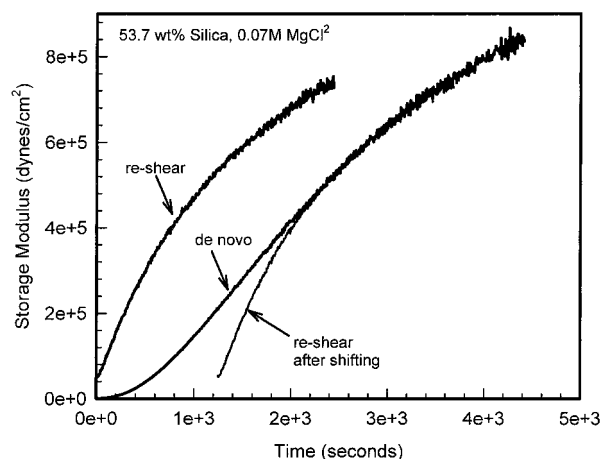


Figure 13. Storage modulus recorded at a frequency of 10 rad/s for 53.7 wt % SiO₂ samples in the presence of 0.07 M MgCl₂ as a function of time after mixing the particles with MgCl₂ solution (curve labeled de novo), and as a function of time after shearing the resultant gelled sample as described in the text (curve labeled reshear). The data points (small circles) are the result of shifting the reshear data by 1240 s along the time axis to allow overlap with the long-time regime of the de novo data.

the last 300 s of the reshear data are approximated by a straight line fit, the slope is approximately 120 dyn/(cm²·s). Although the data for the de novo flocculation were collected for longer times, we can use for comparison the portion of the reshear data encompassing the 300 s period starting at the point where the modulus is approximately 7.1×10^5 dyn/cm², similar to the starting point modulus for the fit applied to the de novo data; this slope is also found to be approximately 120 dyn/(cm²·s). Another way to evaluate the similarity at long times of these data sets is to shift the reshear data along the time axis by an amount that produces coincidence of the long-time regime of both data sets (the shifted data are also shown in Figure 13). This similarity at long times indicates that after the structure is rebuilt to the point that existed before shearing, the structural growth "picks up where it left off". It furthermore suggests that we attain the same type of structure after reshear that was obtained originally during de novo flocculation.

The modulus growth behaviors for silica at 31.7 wt % in 0.05 M MgCl₂ at 25 and 35 °C are shown in Figure 14. These experiments were performed by mixing the particles with appropriate MgCl₂ solution at 25 °C and then transferring the

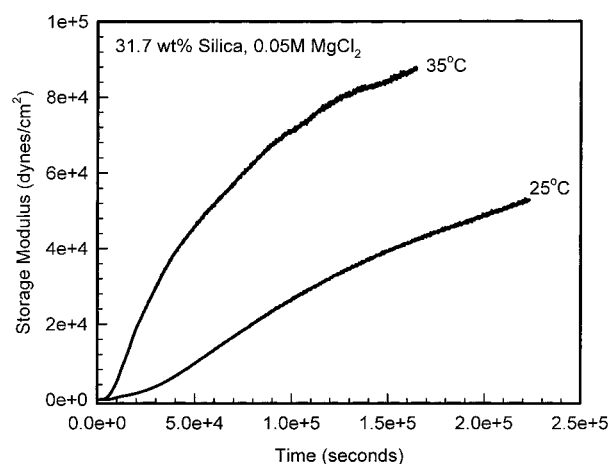


Figure 14. Storage modulus recorded at a frequency of 1 rad/s for 31.7 wt % SiO₂ samples in the presence of 0.05 M MgCl₂ as a function of time after mixing the particles with MgCl₂ solution. Particles were mixed at 25 °C and then transferred to the rheometer for experiments at 25 and 35 °C.

mixed sample to the rheometer which was equilibrated at the desired temperature. The induction period for the sample at 25 °C is approximately 100 min, which, as mentioned earlier, is similar to the time frame within which the SAXS measurements indicate that the evolution of local structure is completed. This observation suggests that the length of the induction period as determined using the rheological data is related to the time needed for the short-range structure to evolve.

The modulus growth rate at 35 °C is greater than that at 25 °C (0.35 dyn/(cm²·s) at 25 °C vs 1.4 dyn/(cm²·s) at 35 °C) because the increased Brownian motion at elevated temperature leads to an increased rate of aggregation. Both sets of data in Figure 14 exhibit the change in slope at long times, which is indicative of the slowing down that occurred just prior to the onset of the quasi-stationary state regime noted in Figure 11 for the 48.5 wt % sample.

The variation in kinetics governing modulus growth (initially slow, fast at intermediate growth stages, slow again in the latter stage of growth) raises the possibility that different mechanisms may operate at early and late stages of the process. Certainly the increase in dynamic moduli reflect the extent of particle aggregation and/or connectivity of the flocculated network. While we lack a reliable model to relate the rheology to specific features of the structure or to the growth mechanism, the activation energy for that mechanism may nevertheless be estimated from the temperature dependence. It may be significant that the initial induction period (prior to acceleration of the modulus growth) conforms approximately to the period of time required to establish a stable local structure according to the SAXS measurements. Regardless of the details, we assume that samples of identical composition flocculated at different temperatures evolve through the same series of intermediate structures with the same dynamic moduli. Accordingly, the activation energy at each isostructural stage of the process may be calculated from the relative rates, for example dG'/dt at each value of G' . Results of this analysis are shown in Figure 15. It is apparent that at all stages of the process, G' grows about 4 times faster at 35 °C than at 25 °C. This corresponds to an activation energy of 105 kJ/mol, or 42 kT at $T = 298$ K. By contrast, according to DLVO theory (Figure 3), the barrier for coupling of an isolated pair should be no more than about 3 kT .

As mentioned earlier, all oscillatory shear experiments were performed in the linear viscoelastic regime for the materials. It

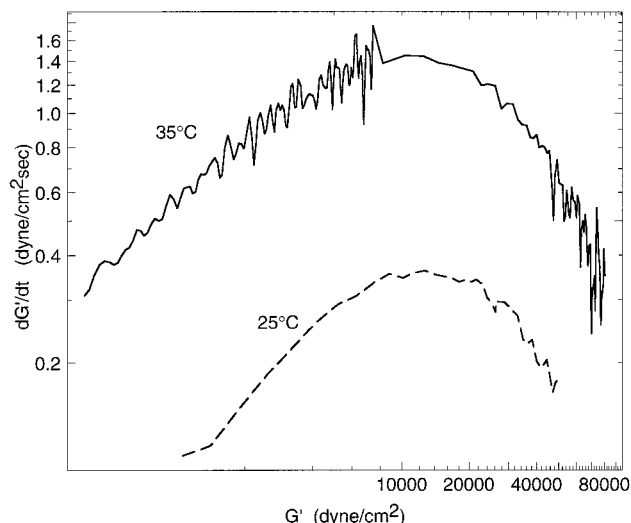


Figure 15. Effect of temperature on the growth rate for the storage modulus G' . Equivalent values of G' are assumed to represent isostructural states in the growth process, such that the relative rates reflect the activation energy.

was important to keep the strain as small as possible for these experiments because the onset of nonlinear viscoelastic behavior was generally detected at strains much less than 1%, which is usual for concentrated flocculated colloids. We were especially careful to make sure that the strains chosen did not disrupt the gel structure as it was forming, a situation which could lead to a perturbation of the measured rate data. This possibility was checked by changing the strain over the range of several tenths of a percent during the time sweep, and confirming that a decrease in the magnitude of the moduli did not occur when the strain was increased. The data discussed in the above paragraphs conformed to this test.

All samples exhibited $G' > G''$ with little or no frequency dependence throughout the flocculation process, characteristics of a viscoelastic solid. The data cannot, however, exclude the possibility of a terminal relaxation time much longer than the longest oscillation period, e.g., 10 min. The increase in G' during flocculation reflects the extent of particle aggregation and/or connectivity of the flocculated network. While we lack a reliable model to relate the rheology to specific features of the structure or to the growth mechanism, the activation energy for that mechanism may nevertheless be estimated from the temperature dependence.

To further characterize the quasi-stationary properties, we examined the long-term stability of the gel volume. Samples of gel were prepared at $\Phi_v = 0.17$ and 0.10, in 0.050 M MgCl_2 , and then allowed to equilibrate with either pure water or excess electrolyte solution at 25 and 50 °C for a period of 48 h. No swelling (or shrinkage) was detected in any of these experiments, confirming that network formation is totally irreversible. Indeed, no syneresis (gel shrinkage or exudation of electrolyte solution) was observed even several months subsequent to the measurements. This observation also demonstrates that the bulk modulus⁴² of the gel network must be significantly larger than the change in osmotic pressure.

7. Discussion

To recapitulate our SAXS and rheology results: for a fresh sample, the first maximum in $g(r)$ becomes sharper and moves to smaller radius over an "induction" period of 60–90 min. Over the same time period, little change is seen in G' and G'' . On time periods longer than 2 h, the SAXS patterns show little

or no change, while the shear moduli increase dramatically. After a longer period on the order of tens of hours, the rate of change for the dynamic moduli becomes progressively slower and can be described as self-limiting. It remains uncertain whether this process converges to any well-defined end point, but nevertheless for practical purposes it exhibits a reproducible stationary state. If these samples are now resheared, their behavior in both SAXS and rheology measurements reverts to that at the end of the induction period. No evidence of syneresis was observed.

The pair distribution $g(r)$ provides quantitative details of particle aggregation and indirect insight into the pair potential. However, any interpretation must make careful allowance for the limits of experimental uncertainty and for complications due to multiparticle correlations. Our SAXS data provide information over a finite length scale, with the largest lengths ($\xi \approx 1500$ – 2000 Å) determined by the smallest angles measured and the shortest length scale ($r_{\min} \approx 150$ – 200 Å) determined by the widest angles measured. As a consequence, our experimentally derived $g(r)$ can neither prove nor exclude the possible existence of a sharp peak due to contacting neighbors at $r = 2R_b = 870$ Å as predicted by the DLVO model (Figure 4a). (The 13 Å variation in R_b introduces a much smaller uncertainty.) For the fully established gels at $\Phi_v = 0.17$ and 0.34 (Figure 7b at 14 h, Figure 9b at 9 h), the first peak in $g(r)$ is centered close to $2R_b = 870$ Å and its width (σ_1) is roughly half that of the smallest measurable distance. From this we may conclude that some of the neighbors bounded by this peak must be in contact with the reference particle, and moreover, within experimental uncertainty, it is possible that all are in contact. Since the total population bounded by the peak (c_1) exceeds 2, the results are compatible with an extended network of primary contacts.

The presence of a strong peak in $g(r)$ in the vicinity of $2R_b$ does not in itself confirm the existence of a local minimum in the pair potential at contact. However, the position and depth of the first minimum do support this conclusion. Qualitatively similar peaks occur in simple fluids with small or nonexistent minima in the pair potential, due simply to the excluded volume of the reference particle.⁴³ In the those cases, propagation of the excluded volume via multiparticle correlation produces a minimum in $g(r)$ at $\geq 2\sqrt{2}R_b$, corresponding to $r \geq 1230$ Å for the particles in our experiments. The observation that the minimum in $g(r)$ for the flocculated gels occurs at much smaller r (ca. 1000 Å) means that some factor beyond correlation effects is responsible for excluding neighbors from this region of space, such as a potential barrier. The presence of such a barrier is also indicated by the fact that this minimum is deeper than in simple liquids, even at much higher Φ_v . For example, in liquid Ar the first maximum and minimum in $g(r)$ are 3.05 and 0.56, respectively,⁴⁴ versus 2.5 and 0.35 for the gel in Figure 7b.

Our SAXS analyses of the flocculated gels do confirm, at least qualitatively, two features of the DLVO pair potential, namely a local minimum near contact and a potential barrier just beyond contact. More extensive scattering data might permit a more rigorous analysis, but the irreversible character of the flocculation process (see below) will preclude solving the statistical mechanics.

The properties of flocculated colloidal gels have generally been measured under what were assumed to be stationary-state conditions, but the true character of that state has not previously been addressed. Our data show a progressive retardation of the flocculation process, ultimately converging to quasi-stationary conditions such that subsequent changes over days or even longer might be regarded as negligible for most practical purposes. We also found that the local structure and rheological

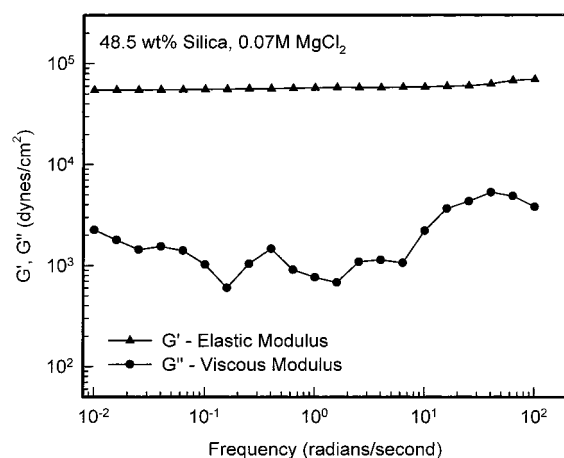


Figure 16. Storage modulus (triangles) and loss modulus (circles) recorded as a function of oscillation frequency for 48.5 wt % SiO_2 particles in the presence of 0.07 M MgCl_2 .

properties stabilized within different time intervals. In gels formed at $\Phi_V = 0.17$ in 0.050 M MgCl_2 at 25 °C the SAXS signal stabilized within a few hours whereas the dynamic moduli continued to evolve for more than 2 days. In order to understand either the evolving or stationary properties, it is essential to identify intrinsic limitations on particle aggregation and network growth, and especially to distinguish between thermodynamic and mechanistic constraints. While the present study does not resolve these issues, certain possibilities can be eliminated.

A significant feature of our experimental system is that the gel volume conformed to the initial volume prior to flocculation under all conditions. If the initial clusters grow with a fractional dimensionality $D = 2$, similar to dilute flocs,¹ then Φ_c , the volume fraction encompassed by clusters, should initially increase to fill the sample volume. Thus if Φ_c grows as $N_c^{3/2}$, where N_c is the average number of particles per cluster, then for a particle volume fraction $\Phi_V = 0.17$ the cluster size need only grow to $N_c = (0.17)^{-2/3} = 3.26$ in order for Φ_c to reach 1. However, it is not obvious why the gel volume does not subsequently shrink or collapse in response to the interparticle adhesive forces. No evidence of syneresis was observed over a period of more than 6 months in samples with Φ_V from 0.17 to 0.34.

Conservation of gel volume may be a consequence of some mechanistic constraint on network growth, or the volume itself may constitute a thermodynamic boundary condition. We considered the possibility that flocculation might involve reversible trapping of particle pairs in a relatively shallow potential minimum, and that the stationary state might represent a dynamic equilibrium with very slow formation and dissociation of adhesive bonds. At equilibrium, contributions from excluded volume and long-range repulsive interactions could result in a positive second virial coefficient causing the gel to expand in order to minimize osmotic pressure. However, as discussed above, no swelling or shrinking of the gel was observed.

If the network is truly irreversible, then the sample should exhibit robust viscoelastic solid behavior in the oscillatory shear spectrum. Figure 16 shows the oscillatory shear moduli as a function of frequency for the sample with 31.7 wt % silica in 0.05 M MgCl_2 . This spectrum was recorded shortly after the completion of the time sweep (at 25 °C) shown in Figure 14. The storage modulus G' is nearly invariant as a function of frequency, and is nearly an order of magnitude larger than G'' over the entire frequency range studied, classic characteristics of a viscoelastic solid. Furthermore, there is no indication of a

terminal relaxation regime (i.e., onset of viscoelastic liquid behavior) even at frequencies as low as 10^{-2} rad/s, again indicative of viscoelastic solid character. Although this behavior does not prove irreversibility beyond time scales represented by the lowest frequency used, these results provide further support for the conclusion stated in the previous paragraph that the network formation is essentially irreversible.

The evolution in $g(r)$ (Figure 7b) shows that early in the process the population of contacting neighbors ($r \approx 850$ Å) grows at the expense of the population just beyond contact ($r \approx 1000$ Å), but little or no further change occurs after about 100 min. As already noted, flocculated clusters are expected to impinge or overlap with one another at a very early stage in their growth; consequently one might expect the gel point to occur well within this period. (This is supported by the observation that $G' > G''$ throughout this period.) Yet the continued increase of G' and G'' over much longer times indicates that the network continues to grow. Rheometry may detect an increase in network connectivity whose effect on the mean coordination number is negligible. For example, at $\Phi_V = 0.17$, each bond within a volume element $1 \mu\text{m}^3$ would only contribute 0.4% to the coordination number.

The modulus growth after reshear does not exhibit the induction period characteristic of the de novo flocculation. This suggests that upon shear the sample is not broken down to individual particles, but rather only clusters of particles that then reassemble upon cessation of shear. Furthermore, the rate of storage modulus growth of the resheared sample becomes similar to that of the de novo sample at late stages, suggesting that the structure achieved upon regrowth of the network is the same as that initially obtained upon addition of salt. This further suggests that the long-range structure is essentially dictated by the initial aggregation of primary particles to doublets, triplets, etc.

Irreversible network growth may be limited by mechanical forces. Once all particles are irreversibly bound to the network, any further coupling requires deformation of the network. This involves stretching and/or bending existing bonds for which the average potential is manifest in the principal elastic moduli. Since the bulk modulus is apparently large enough to suppress volumetric strain, deformation must be confined to deviatoric strain. The associated strain energy should be proportional to the square of the network displacements and to the shear modulus G_e . For example, in the quasi-stationary regime, if we equate G_e with $G' \sim 5$ kPa, and assume that coupling requires interparticle displacements of 100 Å, then the corresponding strain energy is about $27 kT$ at 298 K. This strain energy should contribute to the activation energy for network growth, over and above the barrier for coupling independent particles or clusters. While the magnitude of elastic strain energy is clearly large enough to account for much of the experimentally observed activation energy (section 6), the fact that the latter remains constant over a 50-fold growth in G' suggests that this growth is not directly responsible for suppressing network growth. A more likely scenario might be that the magnitude of G' restricts the coupling reactions to some fraction of potential coupling partners within a suitably small range of separations. As the reaction proceeds and G' grows at the same time, this population of thermally accessible reaction partners becomes vanishingly small.

Acknowledgment. We thank Peter Jernakoff for providing the silica colloids, J. Galperin for the electrokinetic measurements, R. G. Raty for the SEM measurements, and J. England for the light-scattering measurements. P.A.H. was supported by

the MRSEC Program of the National Science Foundation (NSF) under Award No. DMR96-32598. The DND-CAT is supported through E.I. duPont de Nemours & Co., Northwestern University, The Dow Chemical Company, the State of Illinois through the Department of Commerce and the Board of Higher Education (HECA), the US Department of Energy Office of Energy Research, and the US National Science Foundation Division of Materials Research.

Appendix: Formalism Used in the SAXS Data Analysis

In the Born approximation, the scattered X-ray intensity is given by

$$I(\vec{q}) = I_0 \langle |\int d^3r e^{i\vec{q}\cdot\vec{r}} \rho(\vec{r})|^2 \rangle \quad (15)$$

where $\rho(\vec{r})$ is the charge density, the $\langle \rangle$ brackets represent a statistical average, and \vec{q} is the momentum transfer. (In the remainder of the discussion the thermal averages will be implicit.) For a collection of N scattering objects at positions \vec{r}_i embedded in a water medium of constant density ρ_w , we write

$$\rho(\vec{r}) = \rho_w + \sum_{i=1}^N f_i(\vec{r} - \vec{r}_i) \quad (16)$$

If we assume that all the particles are identical, we can then write

$$\int d^3r e^{i\vec{q}\cdot\vec{r}} \rho(\vec{r}) = \int d^3r e^{i\vec{q}\cdot\vec{r}} \rho_w + \sum_i e^{i\vec{q}\cdot\vec{r}_i} \int d^3r e^{i\vec{q}\cdot(\vec{r}-\vec{r}_i)} f(\vec{r}) \quad (17)$$

The ρ_w term gives rise to a $\delta(\vec{q})$ term, i.e., true forward scattering, and can subsequently be ignored. The intensity can be written as in eq 1:

$$I(\vec{q}) = I_0 S(\vec{q}) |F(\vec{q})|^2 \quad (18)$$

$$S(\vec{q}) = |\sum_i e^{i\vec{q}\cdot\vec{r}_i}|^2 = \sum_i \sum_j e^{i\vec{q}\cdot(\vec{r}_i - \vec{r}_j)} \quad (19)$$

$$F(\vec{q}) = \int d^3r e^{i\vec{q}\cdot\vec{r}} f(\vec{r}) \quad (20)$$

Let us first consider the single-particle form factor, $F(\vec{q})$. We will take our particles to be spherical balls of constant density. Because of the spherical symmetry, only the magnitude of \vec{q} is relevant.

$$f(\vec{r}) = \begin{cases} \rho_0 & r \leq R_b \\ 0 & r > R_b \end{cases} \quad (21)$$

with the well-known result²⁰

$$F(\vec{q}) = \frac{4\pi R_b^3 \rho_0}{3} \mathcal{A}(q, R_b) \quad (22)$$

$$\mathcal{A}(q, r) \equiv 3 \frac{\sin(qr) - (qr) \cos(qr)}{(qr)^3} \quad (23)$$

as in eq 5. Here ρ_0 is the difference between the electron density of the spherical ball and that of water. If we had objects that were exactly electron-density-matched to water, we would have no contrast and no scattering.

The above form factor applies for monodisperse spheres. A real colloidal suspension is always composed of particles with

a range of sizes. This dispersion in particle size is also manifested in a dispersion in interaction forces, and in principle an average should be done over the entire Fourier transform of charge density before doing the separation between $|F(q)|^2$ and $S(q)$ in eqs 1 and 18. Indeed, for large polydispersity, failure to do so can introduce substantial errors.^{45,46} However, we make the assumption that the polydispersity can be treated by replacing each particle by an average particle with smeared radius. That is, we replace the squared form factor with a Gaussian average over different radii:^{22-24,28-32}

$$|F(q)|^2 \rightarrow \frac{1}{\sigma_b \sqrt{2\pi}} \int dr e^{-(r-R_b)^2/2\sigma_b^2} \left| \frac{4\pi r^3 \rho_0}{3} \mathcal{A}(q, r) \right|^2 \quad (24)$$

Calculations and measurements on other systems indicate that this approach does not introduce substantial errors if the polydispersity is small enough ($\sigma \leq R_b/10$).^{38,47} In analyzing the data, it was necessary to numerically integrate the above function. This can be efficiently done with the technique of Hermite integration:

$$\int_{-\infty}^{\infty} e^{-x^2} f(x) dx \approx \sum_{i=1}^n w_i f(x_i) \quad (25)$$

where the weights w_i and positions x_i (which are the zeros of Hermite polynomials) are tabulated.⁴⁸ For our calculations we used eq 24 with 10-point Hermite integration, i.e., $n = 10$.

Let us now consider $S(\vec{q})$. We can write $S(\vec{q})$ in the usual way as

$$S(\vec{q}) = \langle n \rangle (1 + \langle n \rangle \int d^3r e^{i\vec{q}\cdot\vec{r}} g(\vec{r})) \quad (26)$$

where $\langle n \rangle$ is the average particle density and $g(\vec{r})$ is the two-particle density-density function. This function has the properties

$$g(\vec{r}) = \begin{cases} 0 & |\vec{r}| \rightarrow 0 \\ 1 & |\vec{r}| \rightarrow \infty \end{cases} \quad (27)$$

It is sometimes more convenient to rewrite

$$g(\vec{r}) = 1 + h(\vec{r}) \quad h(r) = \begin{cases} -1 & r \rightarrow 0 \\ 0 & r \rightarrow \infty \end{cases} \quad (28)$$

$$S(\vec{q}) = \langle n \rangle (1 + \langle n \rangle \int d^3r e^{i\vec{q}\cdot\vec{r}} + \langle n \rangle \int d^3r e^{i\vec{q}\cdot\vec{r}} h(\vec{r})) \quad (29)$$

$$S(\vec{q}) = \langle n \rangle (1 + \langle n \rangle \delta(\vec{q}) + \langle n \rangle \int d^3r e^{i\vec{q}\cdot\vec{r}} h(\vec{r})) \quad (30)$$

Since the $\delta(q)$ term is only manifested in the true forward scattering, we can ignore it. Therefore we take

$$S(\vec{q}) = \langle n \rangle (1 + \langle n \rangle \int d^3r e^{i\vec{q}\cdot\vec{r}} h(\vec{r})) \quad (31)$$

As discussed above, we performed least-squares fits to the entire $I(q)$ data set, allowing free variables in both $|F(q)|^2$ and $S(q)$. For $S(q)$ we chose an empirical function for $h(r)$ which contained the appropriate physical constraints and then calculated $S(q)$ using a combination of analytical and numerical Fourier transforms. $\langle n \rangle h(r)$ was chosen to have the

following form:

$$\langle n \rangle h(r) = D \left(\frac{\text{erf}((r - R_w)/\sigma_w \sqrt{2}) - 1}{2} \right) + A_1 e^{(r-R_1)^2/2\sigma_1^2} + A_2 e^{(r-R_2)^2/2\sigma_2^2} \quad (32)$$

$$S(q) = 1 + S_w(q) + S_{g1}(q) + S_{g2}(q) \quad (33)$$

The first term represents the depletion region around a reference sphere:²¹ two spheres of radius R_b can get no closer to each other than $2R_b$, so around the origin there should be a region of total depletion ($g(0) = 0$, $h(0) = -1$). The form of the error function that we used has the property

$$\left(\frac{\text{erf}(x) - 1}{2} \right) = \begin{cases} -1 & x \rightarrow -\infty \\ 0 & x \rightarrow \infty \end{cases} \quad (34)$$

Thus, in eq 32, D should be numerically equal to the number of scatterers per unit volume, $\langle n \rangle$. We can relate this to the volume fraction of spheres, Φ_V . If Φ_V is the fraction of the total volume occupied by spheres, then we can write it as the number of spheres per unit volume times the volume of each sphere:

$$\Phi_V = \frac{4\pi R_b^3}{3} D \quad (35)$$

In practice, we chose Φ_V to be the fitting parameter, so we took $D = 3\Phi_V/(4\pi R_b^3)$.

The Fourier transform of this “spherical well” is the same calculation we did for the spherical ball. That is, if

$$\langle n \rangle h(r) = \begin{cases} -\langle n \rangle & r \leq R_w \\ 0 & r > R_w \end{cases} \quad (36)$$

then

$$\int d^3r e^{i\vec{q} \cdot \vec{r}} \langle n \rangle h(r) = -\frac{4\pi R_w^3 \langle n \rangle}{3} \mathcal{R}(q, R_w) \quad (37)$$

Using an error function rather than a well with sharp edges is equivalent to using a Gaussian average over radii:

$$\int d^3r e^{i\vec{q} \cdot \vec{r}} h(r) \rightarrow \frac{1}{\sigma_w \sqrt{2\pi}} \int dr e^{-(r-R_w)^2/2\sigma_w^2} \left(-\frac{4\pi R_w^3}{3} \right) \mathcal{R}(q, r) \quad (38)$$

We use the same technique of Hermite integration, giving

$$S_w(q) = -\frac{\Phi_V}{\sqrt{\pi}} \sum_{i=1}^n w_i \mathcal{R}(q, R_w + \sqrt{2}\sigma_w x_i) \quad (39)$$

Although R_w was an unconstrained variable in the fits, we would expect it to be close to double an average sphere radius, $R_w \approx 2R_b$. In fact, it was generally slightly larger than $2R_b$, reflecting perhaps the existence of an additional electrostatic depletion region. Furthermore, the width of the well edge should be greater than or equal to the self-convolution of the sphere polydispersity, $\sigma_w \approx \sigma \sqrt{2}$, on the order of 15–30 Å.

The two Gaussian terms in $\langle n \rangle h(r)$ represent coordination shells. The first one was typically located close to $R_1 \approx 2R_b$, and represented close-contact coordination. The second was located was at larger radius and broader, and accounted for a tail in $g(r)$. We can relate the total coordination in a shell to the

amplitude of the Gaussian by calculating the integral of the volume within the spherical shell. Defining c_i to be the total number of particles within the shell

$$c_i = A_i \int d^3r \exp(-(r - R_i)^2/2\sigma_i^2) \quad (40)$$

$$A_i = \frac{c_i}{4\pi \sqrt{2\pi} \sigma_i (R_i^2 + \sigma_i^2)} \quad (41)$$

We again use Hermite integration when calculating the Fourier transform:

$$S_i(q) = A_i \int d^3r e^{i\vec{q} \cdot \vec{r}} e^{-(r-R_i)^2/2\sigma_i^2}$$

$$S_i(q) = 4\pi A_i \int dr r^2 \left(\frac{\sin qr}{qr} \right) e^{-(r-R_i)^2/2\sigma_i^2} \quad (42)$$

$$S_i(q) = \frac{c_i}{\sqrt{\pi}(R_i^2 + \sigma_i^2)} \sum_{j=1}^n \frac{\sin q(R_i + x_j \sigma_i)}{q} w_j \quad (43)$$

In addition to the “interesting” scattering due to the colloid, there was a small amount of additional background, due to scattering from the air, sample windows, solvent, and also readout noise from the CCD detector. These were collectively modeled by a function $[(Bb(q))^2 + C^2]^{1/2}$, where $b(q)$ was a polynomial in q and $1/q$ whose terms were obtained by least-squares fits to SAXS data from a cell filled with water only, and C was a constant. (The purpose of adding them in quadrature was to ensure that the background function was always positive definite.) Since the sample attenuation could not be calculated precisely (it varied, for example, depending on exactly where the sample was placed on the beam), B and C were unconstrained fitting parameters, but we verified that they converged to “sensible” values.

Putting everything together, we arrive at the function given in eq 7 for the scattered intensity $I(q)$.

References and Notes

- (1) Lin, M. Y.; Lindsay, H. M.; Weitz, D. A.; Klein, R.; Ball, R. C.; Meakin, P. *Proc. R. Soc. London, A* **1989**, *71*, 423, and references therein.
- (2) Yanez, J. A.; Laarz, E.; Bergstrom, L. J. *Colloid Interface Sci.* **1999**, *209*, 162.
- (3) Channell, G. M.; Zukosky, C. F. *AIChE J.* **1997**, *43*, 1700.
- (4) Tadros, Th. F. *Adv. Colloid Interface Sci.* **1996**, *68*, 97.
- (5) Buscall, R.; McGowan, I. J.; Mills, P. D. A.; Stewart, R. F.; Sutton, D.; White, L. R.; Yates, G. E. *J. Non-Newtonian Fluid Mech.* **1987**, *24*, 183.
- (6) Hanley, H. J. M.; Muzny, C. D.; Butler, B. D.; Straty, G. C.; Bartlett, J.; Drabarek, E. *J. Phys.: Condens. Matter* **1999**, *11*, 1369.
- (7) Butler, B. D.; Muzny, C. D.; Hanley, H. J. M. *Int. J. Thermophys.* **1999**, *20*, 35.
- (8) Muzny, C. D.; Butler, B. D.; Hanley, H. J. M.; Agamalian, M. *J. Phys.: Condens. Matter* **1999**, *11*, L295.
- (9) Schaefer, D. W.; Martin, J. E.; Wiltzius, P.; Cannell, D. S. *Phys. Rev. Lett.* **1984**, *52*, 2371.
- (10) Chen, M.; Russel, W. B. *J. Colloid Interface Sci.* **1991**, *141*, 564.
- (11) Scales, P. J.; Johnson, S. B.; Healy, T. W.; Kapur, P. C. *AIChE J.* **1998**, *44*, 538.
- (12) Goodwin, J. W.; Reynolds, P. A. *Curr. Opin. Colloid Interface Sci.* **1998**, *3*, 401.
- (13) DeJaquin, Landau, Verwey, and Overbeek: See Verwey, E. J. W.; Overbeek, J. Th. *Theory of the Stability of Lyophobic Colloids*; Elsevier: Amsterdam, 1948; and Chapters 4 and 5 in ref 5.
- (14) Stöber, W.; Fink, A.; Bohn, E. *J. Colloid Interface Sci.* **1968**, *26*, 62.
- (15) As reported In: *Selected Osmotic Stress Data*; www.mgs1.dcr.nih.gov/docs/osmdata.html, 1996.
- (16) Brinker, C. J.; Scherer, G. W. *Sol Gel Science*; Academic Press: San Diego, 1990; p 624.

- (17) Yoshida, H.; Yamanaka, J.; Koga, T.; Ise, N.; Hashimoto, T. *Langmuir* **1998**, *14*, 569.
- (18) Bird, H. A.; Hutton, J. F.; Walter, K. *An Introduction to Rheology*; Elsevier: New York, 1989, pp 20–21.
- (19) Ferry, J. D. *Viscoelastic Properties of Polymers*, 3rd ed.; John Wiley and Sons: New York, 1980; p 18.
- (20) Guinier, A.; Fournier, G. *Small-Angle Scattering of X-rays*; John Wiley & Sons: New York, 1955.
- (21) Wignall, G. D.; Ramakrishnan, V. R.; Linne, M. A.; Klein, A.; Sperling, L. H.; Wai, M. P.; Gelman, R. A.; Fatica, M. G.; Hoerl, R. H.; Fisher, L. W.; Melpolder, S. M.; O'Reilly, J. M. *Mol. Cryst. Liq. Cryst.* **1990**, *180A*, 25.
- (22) Grunder, R.; Urban, G.; Ballauff, M. *Colloid Polym. Sci.* **1993**, *271*, 563.
- (23) Ballauff, M.; Bolze, J.; Dingenouts, N.; Hickl, P.; Pötschke, D. *Macromol. Chem. Phys.* **1996**, *197*, 3043.
- (24) Megens, M.; van Kats, C. M.; Bösecke, P.; Vos, W. L. *Langmuir* **1997**, *13*, 6120.
- (25) Megens, M.; van Kats, C. M.; Bösecke, P.; Vos, W. L. *J. Appl. Crystallogr.* **1997**, *30*, 637.
- (26) Sirota, E. B.; Ou-Yang, H. D.; Sinha, D. K.; Chaikin, P. M.; Axe, J. D.; Fujii, Y. *Phys. Rev. Lett.* **1989**, *62*, 1524.
- (27) Matsuoka, H.; Harada, T.; Kago, K.; Yamaoka, H. *Langmuir* **1996**, *12*, 5588.
- (28) Korgel, B. A.; Fullam, S.; Connolly, S.; Fitzmaurice, D. *J. Phys. Chem. B* **1998**, *102*, 8379.
- (29) de Kruif, C. G.; Briels, W. J.; May, R. P.; Vrij, A. *Langmuir* **1988**, *4*, 668.
- (30) Hanley, H. J. M.; Straty, G. C.; Lindner, P. *Langmuir* **1994**, *10*, 72.
- (31) Moonen, J.; Vrij, A. *Colloid Polym. Sci.* **1988**, *266*, 1140.
- (32) Lutterbach, N.; Versmold, H.; Reus, V.; Belloni, L.; Zemb, Th. *Langmuir* **1999**, *15*, 337 and references therein.
- (33) Tóth, G. *Langmuir* **1999**, *15*, 6718.
- (34) Dimon, P.; Sinha, S. K.; Weitz, D. A.; Safinya, C. R.; Smith, G. S.; Varady, W. A.; Lindsay, H. M. *Phys. Rev. Lett.* **1986**, *57*, 595.
- (35) Belloni, L. *Chem. Phys.* **1985**, *99*, 43.
- (36) Russel, W. B.; Saville, D. A.; Schowalter, W. R. *Colloidal Dispersions*; Cambridge University Press: Cambridge, New York, 1989.
- (37) Most SAXS samples were prepared de novo immediately before measurement. "Resheared" samples were injected at roughly 0.1 mm/s through a 22-gauge needle immediately before the SAXS measurement.
- (38) Hasmy, A.; Vacher, R.; Julien, R. *Phys. Rev. B* **1994**, *50*, 1305.
- (39) Rieker, T. P.; Misono, S.; Ehrburger-Dolle, F. *Langmuir* **1999**, *15*, 914.
- (40) Alexeev, V. L. *J. Colloid Interface Sci.* **1998**, *206*, 416.
- (41) Freltoft, T.; Kjems, J. K.; Sinha, S. K. *Phys. Rev. B* **1986**, *33*, 269.
- (42) For an isotropic gel the bulk modulus K is related to the elastic shear modulus G_e by $K = 2G_e(1 + n)/3(1 - 2n)$, where n is Poisson's ratio. For the gel network at $\Phi_v = 0.17$ in 0.050 M MgCl_2 , we may approximate G_e by the storage modulus $G' = 5$ kPa (which was frequency-independent but still increasing after 55 h at 25 °C). Assuming $0.5 > n = 0.2$, we obtain $K = 7$ kPa.
- (43) Hansen, J. P.; McDonald, I. R. *Theory of Simple Fluids*, 2nd ed.; Academic Press: London, 1986.
- (44) Yarnell, J. L.; Katz, M. J.; Wenzel, R. G.; Koenig, S. H. *Phys. Rev. A* **1973**, *7*, 2130.
- (45) Frenkel, D.; Vos, R. J.; de Kruif, C. G.; Vrij, A. *J. Chem. Phys.* **1986**, *84*, 4625.
- (46) Krause, R.; D'Aguzzo, B.; Méndez-Alcaraz, J. M.; Nägele, G.; Klein, R.; Weber, R. *J. Phys. Condens. Matter* **1991**, *3*, 4459.
- (47) van Beurten, P.; Vrij, A. *J. Chem. Phys.* **1981**, *74*, 2744.
- (48) Abramowitz, M.; Stegun, I. A. *Handbook of mathematical functions, with formulas, graphs, and mathematical tables*; Dover: Mineola, NY, 1972.